PAPER

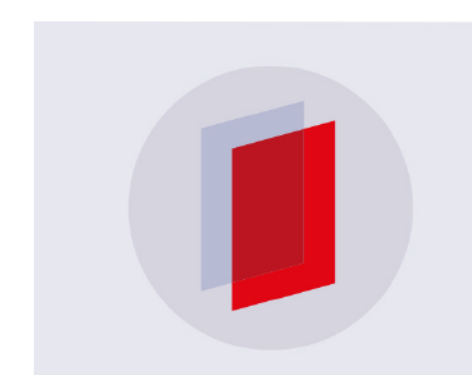
Ultralow thermal conductivity of turbostratically disordered MoSe₂ ultra-thin films and implications for heterostructures

To cite this article: Erik C Hadland et al 2019 Nanotechnology 30 285401

View the article online for updates and enhancements.

Recent citations

 Ultralow shear modulus of incommensurate [SnSe]n[MoSe2]n layers synthesized by the method of modulated elemental reactants Dongyao Li et al



IOP ebooks™

Bringing you innovative digital publishing with leading voices to create your essential collection of books in STEM research.

Start exploring the collection - download the first chapter of every title for free.

IOP Publishing Nanotechnology

Nanotechnology 30 (2019) 285401 (9pp)

https://doi.org/10.1088/1361-6528/aafea2

Ultralow thermal conductivity of turbostratically disordered MoSe₂ ultra-thin films and implications for heterostructures

Erik C Hadland¹, Hyejin Jang², Niklas Wolff³, Robert Fischer¹, Alexander C Lygo¹, Gavin Mitchson¹, Dongyao Li², Lorenz Kienle³, David G Cahill² and David C Johnson¹

E-mail: davej@uoregon.edu

Received 13 November 2018, revised 28 December 2018 Accepted for publication 15 January 2019 Published 25 April 2019



Abstract

Films containing 8, 16, 24, 32 and 64 MoSe₂ layers were synthesized using the modulated elemental reactants method. X-ray reflectivity patterns showed that the annealed films were the targeted number of MoSe₂ layers thick with atomically smooth interfaces. In-plane x-ray diffraction (XRD) scans contained only hk0 reflections for crystalline MoSe₂ monolayers. Specular XRD patterns contained only 00l reflections, also indicating that the hk0 plane of the MoSe₂ layers are parallel to the substrate. Both XRD and electron microscopy techniques indicated that the hk0 planes are rotationally disordered with respect to one another, with all orientations equally probable for large areas. The rotational disorder between MoSe₂ layers is present even when analyzed spots are within 10 nm of one another. Cross-plane thermal conductivities of 0.07–0.09 W m⁻¹ K⁻¹ were measured by time domain thermoreflectance, with the thinnest films exhibiting the lowest conductivity. The structural analysis suggests that the ultralow thermal conductivity is a consequence of rotational disorder, which increases the separation between MoSe₂ layers. The bonding environment of the Se atoms also becomes significantly distorted from C_{3v} symmetry due to the rotational disorder between layers. This structural disorder efficiently reduces the group velocity of the transverse phonon modes but not that of longitudinal modes. Since rotational disorder between adjacent layers in heterostructures is expected if the constituents have incommensurate lattices, this study indicates that these heterostructures will have very low cross-plane thermal conductivity.

Supplementary material for this article is available online

Keywords: TMDs, molybdenum diselenide, thermal conductivity, heterostructures, rotational disorder, turbostratic disorder

(Some figures may appear in colour only in the online journal)

1. Introduction

In the past decade, van der Waals heterostructures have attracted significant research interest [1–4] due to emergent optoelectronic [5–7] magnetic [8, 9] topological [10–12] and

catalytic [13] properties that arise when two or more nanosheets are assembled in a stacked configuration. Depending on the selected constituents, layers can either operate relatively independent of one another [14] or states may be coupled to create novel or modified behavior

¹ Materials Science Institute and Department of Chemistry, University of Oregon, Eugene, OR, United States of America

² Department of Materials Science and Engineering and Materials Research Laboratory, University of Illinois at Urbana-Champaign, Urbana, IL, United States of America

³ Institute for Materials Science, Kiel University, Kiel, Germany

[5, 15, 16]. The modular design of heterostructures enables researchers to vary the constituents, layer thicknesses or stacking sequence to tune a targeted property [2]. More recently there have been efforts to understand more precisely how the rotation angle between layers affects properties and gives rise to extended in-plane structural and electronic superlattices (i.e. Moiré lattices). In transition metal dichalcogenide systems, phenomena dependent on rotation angle include carrier lifetime, collection efficiency, band gap and structural modulations [17–21]. These investigations are particularly relevant to nanoelectronics, where the interactions between constituents become more important as interfaces become a larger fraction of devices [22].

While electronic, optical, and structural changes in single layers and heterostructures of van der Waals materials have been widely studied, there has been much less emphasis on thermal properties. Thermal conductivity between dissimilar materials is an important design parameter in many applications, with high thermal conductivity desired for some (heat dissipation in electronics) and low thermal conductivity desired for others (thermoelectric materials). Theoretical and experimental investigations of the in-plane thermal transport properties of monolayers of transition metal dichalcogenides have yielded a range of in-plane thermal conductivity values for MoS_2 and $MoSe_2$ ($\sim 50-100 \text{ W m}^{-1} \text{ K}^{-1}$) [23–36]. Reported cross-plane thermal conductivities are significantly lower ($\sim 1-4 \text{ W m}^{-1} \text{ K}^{-1}$), reflecting the weak van der Waals bonding between dichalcogenide layers [37]. There are only a few reports on the interfacial thermal conductance between dichalcogenides and substrates or between dichalcogenides and other 2D materials in heterostructures [38-43]. There are conflicting reports of the thermal conductivity Bi₂Te₃-Sb₂Te₃ intergrowths [44-46]. These samples were also structurally ill defined, however, and the degree of intermixing of the cations was not defined in the different samples measured [47]. The small number of reports of the thermal conductivity of van der Waals superlattices is mainly due to the synthetic challenges in preparing these structures via epitaxial growth techniques [48].

The weak van der Waals bonding across the interface also creates the opportunity for an arbitrary rotational angle between two constituents in heterostructures, which significantly impacts physical properties including thermal conductivity. Very low thermal conductivity (0.2 W m⁻¹ K⁻¹) has been reported for heterostructures with periodic TiTe₂-Bi₂Te₃ layers with significant rotational disorder between the constituents [49]. Chiritescu et al reported a 30fold reduction in cross-plane thermal conductivity in WSe₂ compared to bulk single crystal WSe2 due to significant rotational disorder [50]. Surprisingly, significantly higher cross-plane thermal conductivity has been reported in TMDs with extensive defects and non-planar sheets [51]. Electron microscopy studies of the WSe₂ samples used by Chiritescu also indicated extensive defects and non-planar sheets, raising questions as to the cause of the ultralow thermal conductivity [52]. As we discuss in more detail below, we now believe that these early microscopy results were affected by artifacts created by the methods used to prepare the electron microscopy specimens.

In this work we present the synthesis, in-depth structural characterization, and cross-plane thermal conductivity and speeds of sound analysis of MoSe₂ ultra-thin films with targeted thicknesses. Specular x-ray diffraction (XRD) analysis indicates that the films are crystallographically aligned to the substrate and uniform in thickness over a large area (\sim 2 cm \times 2 cm). The spacing between MoSe₂ layers (0.6531 (2) nm) is larger than that reported for the crystalline polymorphs ($\sim 0.646(1)$ nm) for 2H, 3R, or 4H MoSe₂) [53–57]. The measured film thickness is consistent with the targeted integer number of MoSe₂ layers. In-plane diffraction reveals only hk0 reflections of crystalline MoSe₂ and indicates that the MoSe₂ grains are randomly orientated with grain sizes on the order of 10-100 nm. The in-plane lattice parameter is consistent with that reported for single crystals and powders of MoSe₂ prepared at high temperatures. Cross section high angle annular dark field high-resolution scanning transmission electron microscopy (HAADF HRSTEM) reveals flat and parallel MoSe₂ layers with the targeted number of MoSe₂ layers. Plan view transmission electron diffraction patterns indicate that the layers are rotationally disordered from one another. Nanobeam electron diffraction (NBED) patterns and Fourier transform analysis of HRTEM micrographs indicate that the orientations of the layers change over a 10 nm length scale. In-plane electrical conductivity measurements show an activated behavior, with activation energy of 0.2 eV. Crossplane thermal conductivity was evaluated by time domain thermoreflectance (TDTR) and found to be between 0.07 and 0.09 W m⁻¹ K⁻¹, which is more than an order of magnitude smaller than previous reports of crystalline MoSe₂. Previously, the ultralow thermal conductivity of disordered layered materials has been attributed to the combination of turbostratic disorder and pronounced anisotropy in the elastic constants [58] of the parent crystalline solid. Here, we report experimental evidence that the group velocity of the transverse phonon modes is strongly suppressed in the z direction. The suppression of the transverse sound velocity directly reduces the thermal conductivity in the z direction and also enhances the anisotropy of the elastic constants which further suppresses heat conduction due to phonon focusing effects [58]. These results show that ultralow cross-plane thermal conductivity can be achieved in a highly periodic MoSe₂ array in which interlayer rotational disorder is the salient structural feature.

2. Results and discussion

Samples were prepared by depositing a targeted number of Mo|Se bilayers and annealing the samples at low temperatures to crystalize individual MoSe₂ layers and self assemble them into a rotationally disordered stack. Deposition parameters for the modulated elemental precursor were calibrated so that the amount of Mo and Se in a deposited bilayer yielded a 1:2 ratio of the elements. These values were adjusted during this study to yield precursors with varying

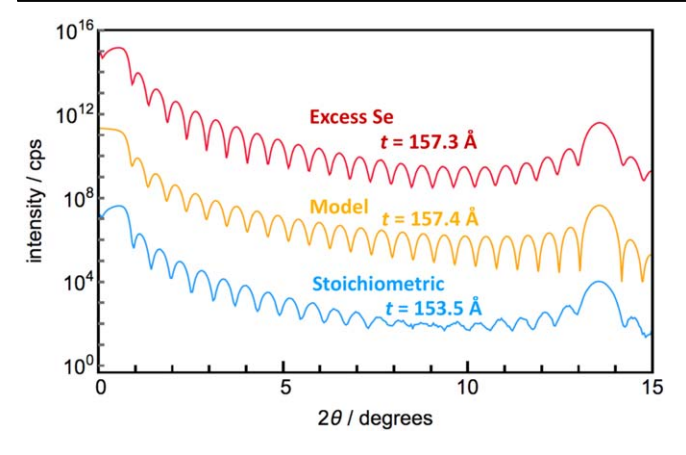


Figure 1. Low-angle reflectivity patterns for two samples designed to form 24 layers of $MoSe_2$. The yellow trace (middle) is a calculated pattern that was used as a comparison for the two experimental patterns (red and blue). The blue (bottom) trace was annealed from a stoichiometric precursor with $\sim 5\%$ deficiency in Mo, whereas the red trace (top) contained a $\sim 10\%$ Se excess and the correct amount of Mo to form 24 layers. XRF data indicated that the films after annealing had the same composition.

amounts of excess Se as this improved the quality of the resulting XRR and XRD patterns. The thickness of the deposited layers was then scaled so the number of atoms in each Mo|Se bilayer matched the number of atoms in a single Se–Mo–Se trilayer of MoSe₂ (subsequently called a monolayer). Samples were prepared with a range of total thicknesses by varying the number of Mo|Se bilayers deposited. Samples were annealed at 650 °C for 60 min in a N₂ atmosphere followed by a 60 min anneal at 550 °C in a sealed tube with a Se partial pressure. The specular diffraction patterns of all samples contained only the 00*l* reflections expected for MoSe₂ indicating that the MoSe₂ planes are parallel to the substrate.

Figure 1 contains both calculated (yellow) and experimental (blue and red) low-angle reflectivity patterns of samples where 24 MoSe₂ monolayers were targeted. The patterns contain periodic oscillations called Kiessig fringes, which result from two superimposed phenomena—the interference of scattered x-rays off the top and bottom interfaces of the film and the incomplete destructive interference of the 24 MoSe₂ monolayers. The position of the Kiessig fringes at low angles is dominated by the reflectivity of the sample, and their location depends the average total film thickness via Bragg's law corrected for refraction. The position of the Kiessig fringes closer to the 001 Bragg reflection for MoSe2 is dominated by the incomplete destructive interference of the finite size crystal, and their location is related to the number of monolayers and their spacing, which is the c-axis lattice parameter. The annealed film from the stoichiometric precursor (blue) was ∼1 nm thinner than the target thickness, leading to a film with less than 24 layers of MoSe₂. There is a difference between the thickness calculated from the position of the low-angle Kiessig fringes (between 22 and 23 monolayers) and the higher angle fringes near the Bragg reflection (23 monolayers), indicating that different regions of the film have slightly different thicknesses. The interference between

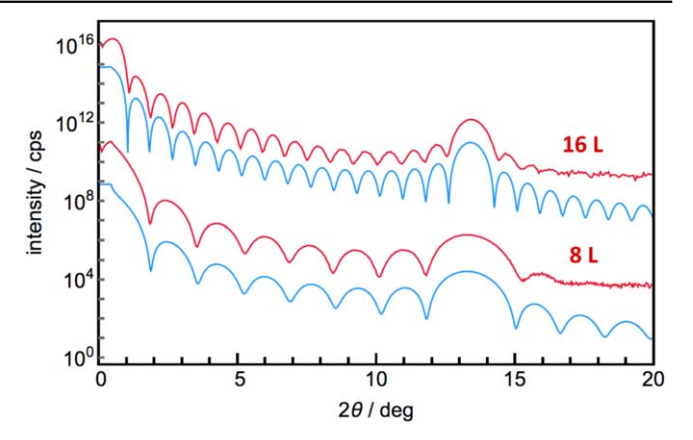


Figure 2. Low-angle reflectivity patterns of 8- and 16-layer $MoSe_2$ films that show strong agreement between the calculated (blue) and experimental (red) traces. The scans are offset for clarity.

these two areas of the film results in a reduction in the amplitude of the Kiessig fringes between 7° and 10° relative to that in the calculated pattern. Precursors deposited with the correct amount of Mo but a 10%-15% excess of Se form films with Kiessig fringe amplitudes closer to that expected from the calculation; and the excess Se is expelled upon annealing as monitored using x-ray fluorescence spectroscopy (XRF) [59]. The agreement between the experimental (red) and calculated (yellow) reflectivity patterns indicates that this sample contains 24 parallel monolayers, which is consistent with the cross-sectional STEM images discussed later. The samples used in this study were all prepared from precursors with $\sim \! 10\%$ excess Se.

Films containing 8–64 monolayers of $MoSe_2$ were prepared by changing the number of Mo|Se bilayers deposited in the precursor. Figure 2 contains the experimental and calculated x-ray reflectivity patterns for 8- and 16-layer structures. The agreement between the experimental (red) traces and calculated (blue) traces demonstrates the ability to prepare films with a targeted number of $MoSe_2$ monolayers over the entire probed area ($\sim 4 \, \mathrm{cm}^2$). The Parratt relationship relates the angle to which resolved fringes are observed to how parallel the bottom and top surfaces of the sample are over the probed area [60]. The observation of fringes to $2\theta > 15^\circ$ indicates sub-Angstrom smoothness.

Specular diffraction patterns were collected to determine the out-of-plane structure of the samples. All the observed Bragg maxima (figure 3) can be indexed as the 00l series of reflections, indicating that the MoSe₂ layers are parallel to the substrate. Rocking curve measurements were done on the 00l reflections to measure the extent of preferred alignment, yielding half widths of 1.1° θ . These half widths are significantly narrower than the $\sim 15^{\circ}$ θ reported by Muratore et al [51]. The line widths of the reflections broaden as the number of layers decreases and the coherence length becomes limited by the film thickness. c-axis lattice parameters were calculated for the different samples (see table 1), yielding an average value of 0.6531(2) nm, which is larger than the individual layer thicknesses calculated from previously reported c-axis lattice parameters (0.646(1) nm) for 2H, 3R,

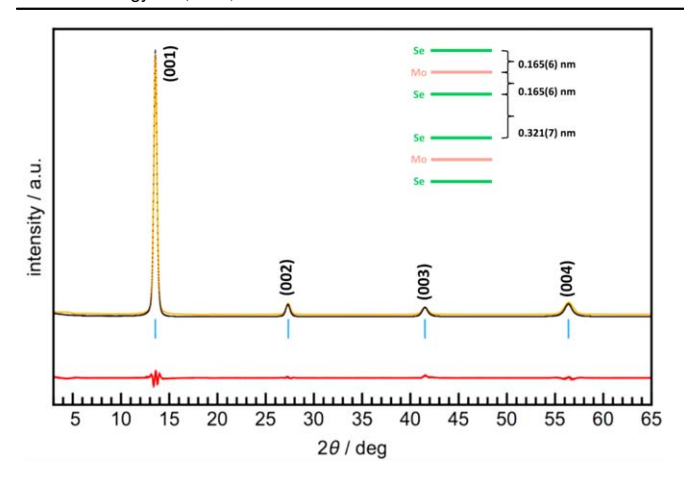


Figure 3. Specular diffraction patterns show only the 00*l* series of Bragg reflections, indicating that MoSe₂ nanosheets run parallel to the substrate. The structural refinement shows a slightly increased interplanar distance between Se and Mo planes, which is consistent with other low temperature syntheses. Experimental data points are shown in black, and the refinement is shown in yellow. The residuals are in red.

or 4H MoSe₂ prepared by high temperature syntheses [53–57]. We believe that this increased thickness per MoSe₂ trilayer is a consequence of the rotational disorder between adjacent MoSe₂ layers. Even larger thicknesses per MoSe₂ trilayer have been reported for MoSe₂ prepared using a variety of low T synthesis techniques [61–63]. The larger thicknesses from these syntheses were not explicitly discussed, but for some approaches may be a consequence of included solvent molecules between the MoSe₂ layers.

Rietveld refinement of the specular diffraction pattern of the MoSe₂ sample with 64 layers was conducted to gain insight into the cause of the expanded c-axis lattice parameter. Figure 3 contains the experimental and calculated diffraction patterns, with a schematic of the refined model inset within the figure. The van der Waals gap from our refined model, taken as the distance between the Se planes in adjacent MoSe₂ layers, 0.321(1) nm, is 0.008 nm larger than that reported in the literature for MoSe₂ prepared at high temperatures (0.3128 nm). The Se–Mo interatomic distance (0.165(7) nm) is also larger than that reported in the literature for the thermodynamically stable product (0.1615(1) nm). Our XRF analysis indicates that the stoichiometry of all the samples prepared is MoSe_{1.99(2)} [59] indicating that large deviations from stoichiometry (due to Se loss, for example) are not responsible for these differences. The increase in the c-lattice parameter is a consequence of both of these distances increasing, which we speculate is caused by the rotational disorder between adjacent MoSe₂ layers.

Grazing-incidence XRD was collected to obtain information about the in-plane structure of the samples. All of the patterns contain Bragg maxima that can be indexed as *hk*0 reflections using a hexagonal unit cell (figure 4), consistent with the preferred orientation of MoSe₂ layers. The *a*-axis lattice parameters of the different MoSe₂ films were determined using LaBail fits of the diffraction patterns. The value obtained, 0.331(1) nm, agrees with literature values for

MoSe₂, which range from 0.329 nm for MoSe₂ prepared at high temperature [54–57] to as low as 3.22 for films prepared at low temperature [7]. The Debye–Scherrer equation was used with line widths obtained from the LaBail fits to obtain an estimate of 10 nm for the in-plane grain sizes [64]. In-plane pole figures indicate that the crystallites are randomly oriented in the xy-plane over the \sim 4 cm² analytical area.

Cross-sectional HAADF HRSTEM images were collected to gain additional information about the structure of the MoSe₂ layers and their stacking. Figure 5 shows images of the 8- and 24-layer samples, which contain layers of alternating contrast corresponding to the nanosheets (bright) and van der Waals gaps (dark) with the layers parallel to the substrate. The number of Mo|Se layers in the precursors has been retained in the crystalized films, which contain parallel layers and atomically sharp interfaces in agreement with the diffraction data discussed previously. Areas with resolvable zone axes are not frequent and neither are areas with alignment between layers, such as that in the image of the 8-layer sample. This is consistent with the rotational disorder previously reported from other films made via modulated elemental reactant (MER) synthesis and the pole figure measurements discussed earlier. A periodic stacking of the layers observed in the thermodynamically stable bulk phases of MoSe₂ is not observed. A non-representative area of the 8-layer film is shown in figure 5 because it contains a rare region where the bottom 2 layers have a [110] orientation while layers 3 and 4 have the [100] axis aligned with the beam. The observed chevron arrangement of the atoms within the MoSe₂ nanosheets where the electron beam is aligned down the [100] axis is consistent with trigonal prismatic coordination of the Mo atoms. Layers 5-8 do not show resolvable low index zone axes, indicating that they possess different rotational orientations. Most of the areas viewed in the STEM investigation did not show any, or at most a single layer with a resolvable zone axis. A high density of independent nucleation sites probably causes the rotational disorder between layers during the self-assembly of the precursor. Faster growth along a MoSe2 sheet than heterogeneous nucleation of an adjacent layer at the interface of an existing layer results in the random rotational orientation. Grain sizes within a layer agree with the diffraction estimates using Debye–Scherrer analysis (on the order of \sim 10 nm).

The HAADF HRSTEM images in figure 5 consist of well-defined planar layers. These images are very different from previously reported HAADF HRSTEM images of WSe₂ made by MER synthesis, where the cross section high-resolution TEM images showed non-planar layers with small inplane grain sizes [52]. These cross-sectional images of WSe₂ were inconsistent with the reported XRD data on the same sample [50] indicating that the sample was probably damaged during TEM sample preparation.

Plan view HRTEM data and NBED patterns were collected over a 250×250 nm region of the 8-layer sample to obtain information on the local rotational disorder. Figure 6 shows a representative 3×3 grid of these NBED patterns collected with a focused 8 nm electron beam on a square grid with 10 nm between the centers of the electron beam. All of

Table 1. Summary of lattice parameters from x-ray diffraction, cross-plane thermal conductivity (Λ), and z-axis longitudinal (C_{33}) and shear (C_{44}) elastic constants for the rotationally disordered MoSe₂ films in this study.

# MoSe ₂ layers	a (nm)	c(nm)	$\Lambda(W~m^{-1}K^{-1})$	C_{33} (GPa)	C ₄₄ (GPa)
64	0.3309(5)	0.6532(2)	$0.090^{+0.004}_{-0.002}$	44 ± 3	_
32	0.3313(1)	0.6526(2)	$0.07^{+0.012}_{-0.002}$	32 ± 5	_
24	0.3309(1)	0.6528(5)	$0.07^{+0.02}_{-0.002}$	41 ± 7	_
16	0.3310(1)	0.6536(9)	$0.07^{+0.03}_{-0.004}$	38 ± 8	_
8	0.3308(4)	0.653(1)	_	_	_
≈ 92	_	_		33 ± 1	3.0 ± 0.9

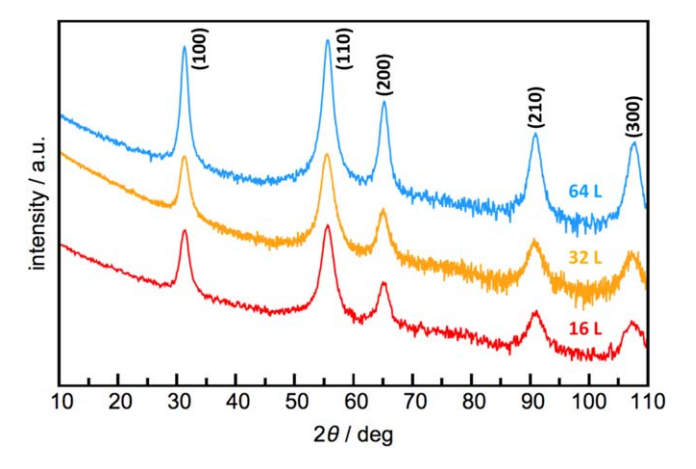
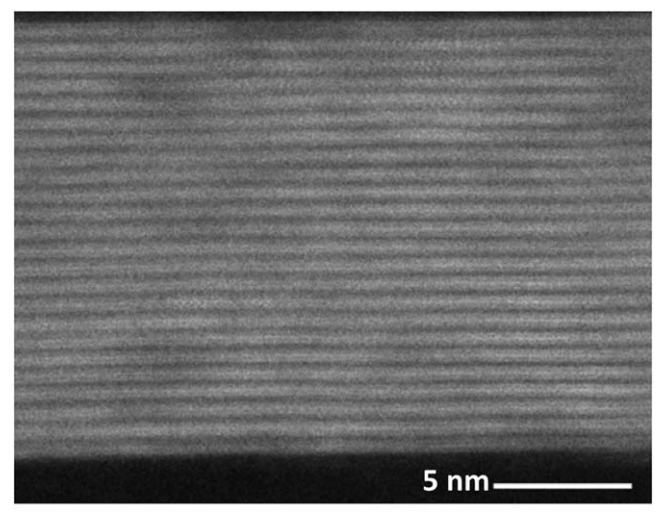


Figure 4. Representative GIXRD patterns of 16-, 32-, and 64-layer films showing only hk0 reflections due to the preferred orientation of the crystallites.

the patterns contain multiple hexagons of varying orientation and intensity, reflecting the local orientations of the hexagonal MoSe₂ basal planes. The local orientations change significantly from spot to spot. The grain orientations are randomly distributed and they change intensity independently of one another, consistent with the rotational disorder inferred from the cross section HRSTEM data discussed earlier. If all of the patterns over the 250×250 nm area are stacked on top of one another, rings of uniform diffraction intensity are obtained (see SI, available online at stacks.iop.org/NANO/ 30/285401/mmedia), consistent with the x-ray pole figure experiment discussed earlier. Different grain orientations can be identified in each individual pattern, and are represented by the different color hexagons in the central pattern of figure 6. These orientations were tracked from the central pattern to the adjacent regions. If a specific orientation is still observed, a hexagon of that color is shown. If the orientation is missing in an adjacent region, the hexagon is not shown. While a specific orientation may exist on diffraction patterns collected on adjacent spots, the majority of the orientations change even at this length scale.

Further information about the extent of rotational disorder of the $MoSe_2$ layers on a smaller scale was obtained through the evaluation of fast Fourier transforms (FFTs) taken from 5×5 nm² region of the HRTEM micrograph depicted in figure 7 and explained in the SI. The rotational disorder of NBED patterns on the larger scale is consistent with the superposition phase contrast visible in figure 7(a). However,



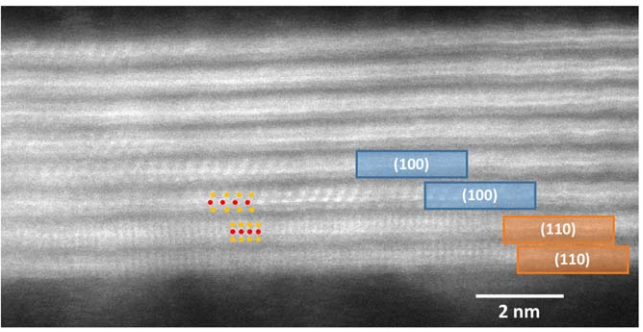


Figure 5. Cross-sectional HAADF-STEM images of 24-layer and 8-layer MoSe₂ films. Grain orientations and zone axes are indicated in the shaded boxes, and the arrangement of atoms is shown with red spheres corresponding to Mo atomic columns and gold spheres corresponding to Se atomic columns.

confined areas with single rotational alignment could be identified, see, HRTEM contrast and FFT data evaluation showing single hexagon patterns in figures 7(b) and (c), respectively. To show how the orientations of the hexagons vary as a function of location, we created a color coded map of the hexagon orientations (figure 7(d)), similar to the colored hexagons of figure 6. In figure 7(d), the colors refer to specific rotational orientations observed in this area. New orientations appear and rotations from an adjacent square disappear as the FFT area is moved across the image. Specific orientations persist over 10–30 nm length scales, as observed for the sample area examined by NBED. Details of the data evaluation are presented in the supporting material. The changes in grain orientation observed in figure 7 are

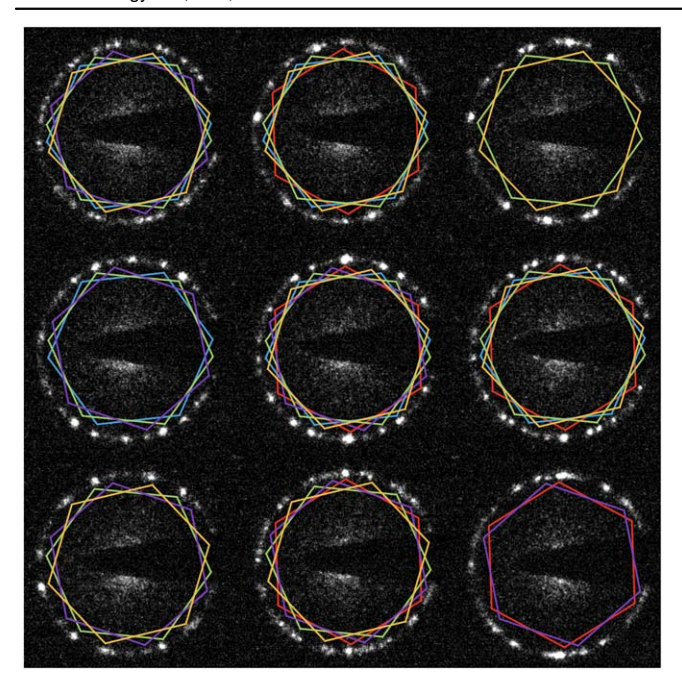


Figure 6. Nanobeam electron diffraction patterns of selected areas of MoSe₂ separated by 10 nm. Grain orientations are highlighted by colored hexagons in the central SAED image. If one of these orientations persists in a neighboring SAED image, the color hexagon corresponding to that orientation is superimposed on the image.

consistent with the estimates of the in-plane grain size and illustrate the extensive local rotational disorder between MoSe₂ layers on the nanometer scale.

Electrical resistivity was measured at temperatures between 165 and 295 K using the van der Pauw method. The resistivity increased exponentially from $0.83\,\Omega$ m at room temperature to $10.7\,\Omega$ m at 165 K, indicating that the films are semiconducting. A linear regression of $\ln\rho$ v. T^{-1} (figure 8) yielded an activation energy of ~ 0.2 eV over this small temperature range, which is approximately one order of magnitude smaller than the optical band gaps reported for bulk 2H MoSe₂ and large-grain monolayer structures [65]. While studies report a narrowing of band gaps in rotationally disordered systems by $\sim 15\%$ [17] the lower activation energy in our system obtained from the resistivity suggests that we are not observing the intrinsic band gap, but instead we are measuring barriers introduced by the grain boundaries or the activation energy of a defect band [66].

Thermal conductivity measurements were made using the TDTR method [67] on the 16, 24, 32, and 64-layer films with a 80 nm thick aluminum film as an optical transducer sputtered on the $MoSe_2$ films. The 8-layer film was not measurable as it is too thin for the measurement to have enough sensitivity to the thermal conductivity. The thermal model is compared with the measured TDTR data to determine the thermal conductivity of $MoSe_2$ (Λ). Regarding the other parameters of $MoSe_2$ that are needed for the thermal model, we used the heat capacity as $1.89 \, \mathrm{J \, K^{-1} \, cm^{-3}}$ [68]; for the interfacial thermal conductance (G) between Al and $MoSe_2$, we assume the range of G as $100 \pm 70 \, \mathrm{MW \, m^{-2} \, K^{-1}}$. The

lower end corresponds to the lowest interfacial thermal conductance of metals and van der Waals materials, i.e. NbV and ReS₂ [68]. The upper end corresponds to the interfacial thermal conductance of Al sputtered on Si thermal oxide. The TDTR signal is most sensitive to Λ of MoSe₂ and less sensitive to G, and only the lower end of G affects the fitted G. A summary of the thermal conductivity of 16, 24, 32, and 64-layer films is given in table 1. Note that the positive uncertainty of G corresponds to G = 30 MW m⁻² K⁻¹ and the negative uncertainty corresponds to G = 170 MW m⁻² K⁻¹.

The measured cross-plane thermal conductivities, 0.07-0.09 W m⁻¹ K⁻¹, are extremely low for a fully dense solid. These values are a factor of 20-50 smaller than what has been reported for bulk dichalcogenides of Mo, W, and Ti for which values ranged from $1.75~W~m^{-1}~K^{-1}$ for a purchased single crystal of WSe₂ to $4.7~W~m^{-1}~K^{-1}$ for a natural mined single crystal of MoS₂ [35, 37, 50, 51, 69]. Thermal conductivity values for crystals of Mo and W dichalcogenides grown via vapor transport range from a low of 1.2 W m⁻¹ K⁻¹ for WSe₂ to a high of 3.5 W m⁻¹ K⁻¹ for MoSe₂ [37, 70, 71]. Samples of MoS₂ prepared by annealing Mo films in S vapor have thermal conductivities close to those of bulk crystals [51, 72]. These values are generally in agreement with calculated values [73, 74]. Intercalation has been shown to lower the cross-plane thermal conductivity of dichalcogenides by a factor of 2–3 [69, 72] significantly less than the reduction observed here. Very low cross-plane thermal conductivities have been published for disordered dichalcogenide films prepared by magnetron sputtering, $0.1-0.3 \text{ W m}^{-1} \text{ K}^{-1}$ [51]. Models that accommodate reduced symmetry along z have corroborated that stacking disorder and lattice expansions on the order of 2%-3% can reduce cross-plane thermal conductivity to $\sim 0.4 \,\mathrm{W \, m^{-1} \, K^{-1}}$ [75].

The longitudinal speed of sound along the z-axis (v_L) of the Al-sputter coated MoSe₂ films can be determined by using picosecond acoustics [76]. The longitudinal elastic constant, C_{33} , can be calculated as $C_{33} = \rho v_L^2$, where ρ is the theoretical mass density of MoSe₂, 7.0 g cm⁻³, and is shown in table 1. The C_{33} of 32–44 GPa is comparable to that of other transition metal dichalcogenides, e.g. 52 GPa for MoS₂ bulk [72] and 43 GPa for ReS₂ exfoliated flake [77].

We also determined transverse speed of sound along the z-axis (v_T) via surface acoustic wave measurements [78]. The measurement can be performed in the same setup as TDTR but requires a thicker film with a tuned thickness of Al transducer. Therefore, we used a MoSe₂ film prepared by the MER method but of 60 nm thickness (\approx 92 layers). The sample was coated with 145 nm thick Al. Surface acoustic waves with a wavelength of 700 nm were generated using an elastomeric polydimethylsiloxane phase-shift mask attached onto the sample surface. The shear modulus (C_{44}) was derived from the measured frequency of the surface acoustic waves, from which the transverse speed of sound along the z-axis can be calculated using $C_{44} = \rho v_T^2$.

The shear modulus of the $60\,\mathrm{nm}$ thick $MoSe_2$ film is $3.0\pm0.9\,GPa$ (see table 1). To the best of our knowledge, this is the first experimental data for the shear modulus of a disordered van der Waals material. This value is significantly

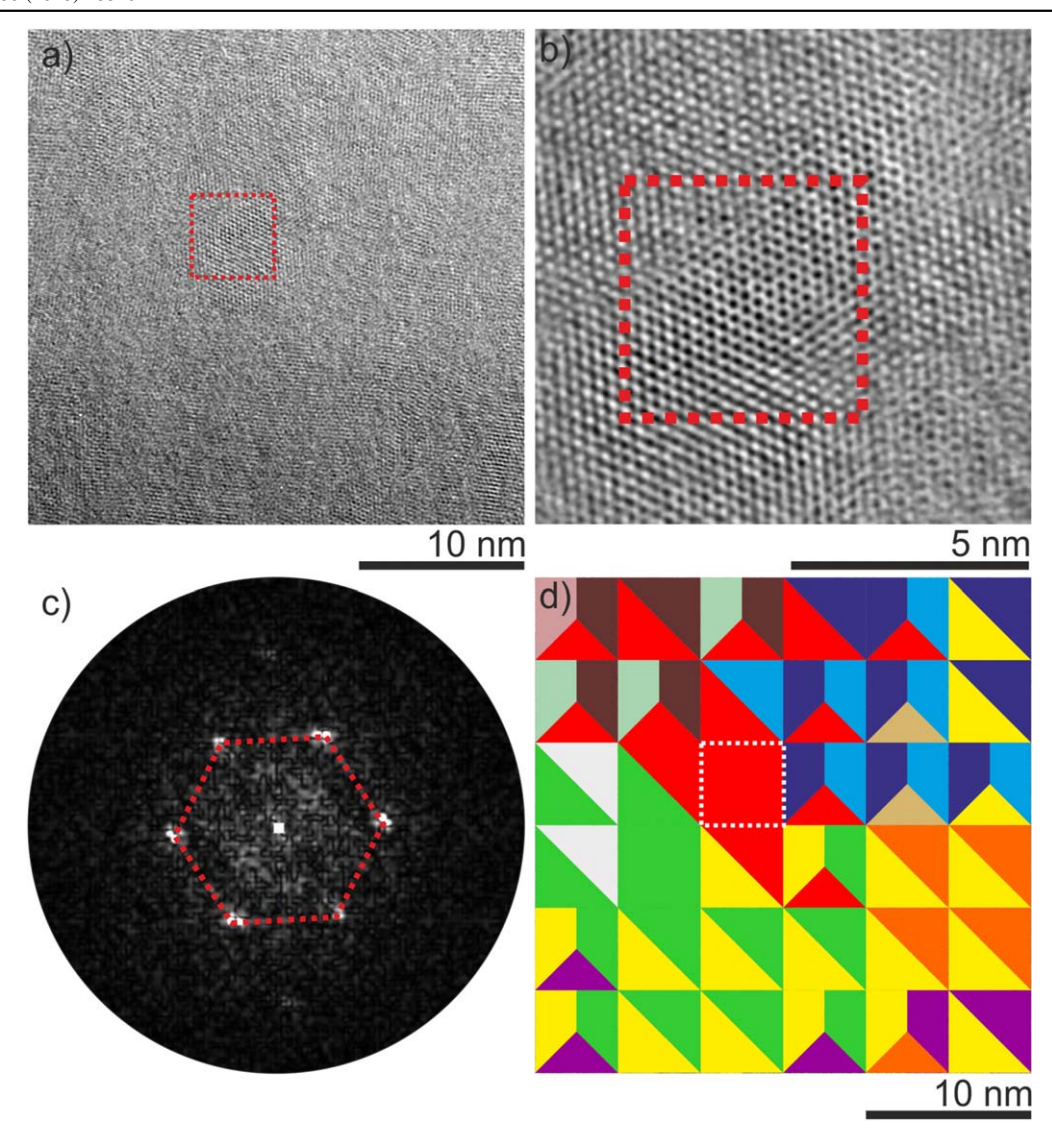


Figure 7. Plan view HRTEM study of the 8-layer $MoSe_2$ sample. (a) HRTEM micrograph showing blurred phase contrast originating from the superposition of rotationally disordered layers. (b) Magnified view of the red box in (a) showing a small area with single rotational alignment, and corresponding FFT pattern (c). (d) Color coded map showing different hexagon orientations extracted from a grid of FFTs from $36 \times 5 \times 5$ nm² square areas. The presentation is limited to the three most prominent rotations.

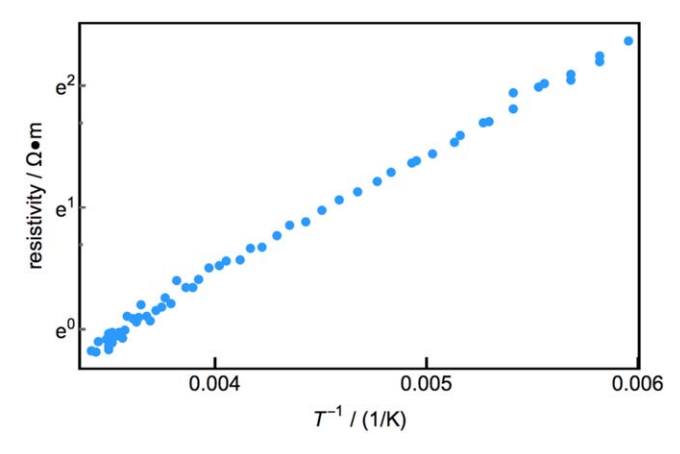


Figure 8. The linear relationship between $\ln \rho$ and T^{-1} indicates that films are semiconducting.

suppressed compared with the bulk counterpart: although direct experimental results are not available, the shear modulus derived from the frequency of Raman-active shear modes is 17–19 GPa for MoSe₂ and 19 GPa for MoSe₂ [79]. First-principles calculations predict 33 GPa for MoSe₂ [80] although we point out that this result is likely to be sensitive to the choice of the functionals used to describe the van der Waals interactions between the layers. The reduced shear modulus implies that the ultralow thermal conductivity of the rotationally disordered MoSe₂ films can be partly attributed to the strongly suppressed group velocity of transverse acoustic phonon modes.

Results presented in this study suggest that rotational disorder in otherwise well-defined crystalline systems is sufficient to reduce thermal conductivity to ultralow values. The structural analysis indicates that our films consist of a highly periodic MoSe₂ array with flat (non-wavy) monolayers that have in-plane lattice parameters equal to that found in

crystalline MoSe₂. The in-plane XRD pole figures show that the layers have a random rotational orientation over the large area probed. The NBED and high-resolution TEM imaging show that this interlayer rotational disorder exists at the nanoscale. The c-axis lattice parameter, however, is $\sim \!\! 1\%$ larger than that measured in crystalline MoSe₂ due to the rotational disorder between the layers.

The ultralow thermal conductivity values reported here are consistent with the cross-plane thermal conductivities reported for WSe₂ and dichalcogenide containing heterostructures prepared using the MER approach with semi-conducting rock salt layers, with values ranging from 0.05 to 0.35 W m⁻¹K⁻¹ [49, 50, 81–84]. From the acoustic measurements, we reveal that the rotational disorder suppresses the group velocity of the transverse phonon modes along the *z*-axis, while that of the longitudinal modes remain intact.

3. Summary

The results presented herein are relevant for researchers investigating the potential use of the novel properties found in van der Waals heterostructures for use in nanoelectronic applications where interfaces between layers are likely to be a large fraction of the active devices. We showed via extensive structural characterization that rotational misalignment between layers creates very anisotropic environment in the xy plane for the chalcogen atoms of dichalcogenides, as the chalcogen atom in one layer is no longer sitting in the middle of a triangle of chalcogen atoms from the adjacent layer [85]. This rotational disorder results in extremely low thermal conductivities for a fully dense solid. Similar anisotropic environments are present at the interfaces in van der Waals heterostructures due to the different in-plane lattice parameters of the constituents. Consequently, we expect that van der Waals heterostructures will likely have very low crossplane thermal conductivities. This will be an important design issue for heterostructures devices that dissipate power and a potential opportunity to obtain high thermoelectric performance in devices operating across the van der Waals interfaces of heterostructures.

Acknowledgments

The authors acknowledge support from the National Science Foundation under grant DMR-1710214 and the German Research Foundation (DFG) under grant CRC1261-A6. We would like to acknowledge the Center for Advanced Materials Characterization in Oregon (CAMCOR) at the University of Oregon. Additionally, we would like to acknowledge the National Center for Electron Microscopy at Lawrence Berkley National Lab and Christoph Gammer for encoding software to acquire the nanobeam electron diffraction data. Work at the Molecular Foundry was supported by the Office of Science, Office of Basic Energy Sciences, of the US. Department of Energy under Contract No. DE-AC02-05CH11231. Thermal conductivity measurements and

analysis were carried out in the Frederick Seitz Materials Research Laboratory Central Research Facilities, University of Illinois, and were supported by NSF EFRI-1433467.

ORCID iDs

Erik C Hadland https://orcid.org/0000-0002-2205-4363 Niklas Wolff https://orcid.org/0000-0002-8796-0607

References

- [1] Novoselov K S, Mishchenko A, Carvalho A and Castro Neto A H 2016 *Science* **353** 6298
- [2] Geim A K and Grigorieva I V 2013 Nature 499 419-25
- [3] Hamann D M, Hadland E C and Johnson D C 2017 Semicond. Sci. Technol. 32 93004
- [4] Lin Z et al 2016 2D Mater. 3 42001
- [5] Rivera P et al 2015 Nat. Commun. 6 6242
- [6] Hong X, Kim J, Shi S-F, Zhang Y, Jin C, Sun Y, Tongay S, Wu J, Zhang Y and Wang F 2014 Nat. Nanotechnol. 9 682-6
- [7] Zhou X et al 2017 2D Mater. 4 25048
- [8] Jiang S, Shan J and Mak K F 2018 Nat. Mater. 17 406–10
- [9] Kim H H, Yang B, Patel T, Sfigakis F, Li C, Tian S, Lei H and Tsen A W 2018 Nano Lett. 18 4885–90
- [10] Kou L, Wu S-C, Felser C, Frauenheim T, Chen C and Yan B 2014 ACS Nano 8 10448–54
- [11] Rajput S, Li Y-Y, Weinert M and Li L 2016 ACS Nano 10 8450-6
- [12] Märkl T, Kowalczyk P J, Le Ster M, Mahajan I V, Pirie H, Ahmed Z, Bian G, Wang X, Chiang T-C and Brown S A 2017 2D Mater. 5 11002
- [13] Deng D, Novoselov K S, Fu Q, Zheng N, Tian Z and Bao X 2016 Nat. Nanotechnol. 11 218–30
- [14] Tongay S et al 2014 Nano Lett. 14 3185-90
- [15] Ohta T, Robinson J T, Feibelman P J, Bostwick A, Rotenberg E and Beechem T E 2012 Phys. Rev. Lett. 109 186807
- [16] Fang H et al 2014 Proc. Natl Acad. Sci. USA 111 6198-202
- [17] Zhang C, Chuu C-P, Ren X, Li M-Y, Li L-J, Jin C, Chou M-Y and Shih C-K 2017 Sci. Adv. 3 e1601459
- [18] Liu K et al 2014 Nat. Commun. 5 4966
- [19] Wang K et al 2016 ACS Nano 10 6612-22
- [20] Kang J, Li J, Li S S, Xia J B and Wang L W 2013 *Nano Lett.* 13 5485–90
- [21] Heo H et al 2015 Nat. Commun. 6 7372
- [22] Goyal V and Balandin A A 2012 Appl. Phys. Lett. 100 73113
- [23] Hong Y, Zhang J and Zeng X C 2016 J. Phys. Chem. C 120 26067–75
- [24] Peng B, Zhang H, Shao H, Xu Y, Zhang X and Zhu H 2016 RSC Adv. 6 5767–73
- [25] Kandemir A, Yapicioglu H, Kinaci A, Çağın T and Sevik C 2016 Nanotechnology 27 55703
- [26] Norouzzadeh P and Singh D J 2017 Nanotechnology 28 75708
- [27] Wang H, Qin G, Li G, Wang Q and Hu M 2017 2D Mater. 5 15022
- [28] Jiang J-W, Park H S and Rabczuk T 2013 J. Appl. Phys. 114 64307
- [29] Liu X, Zhang G, Pei Q-X and Zhang Y-W 2013 Appl. Phys. Lett. 103 133113
- [30] Li W, Carrete J and Mingo N 2013 Appl. Phys. Lett. 103 253103
- [31] Gu X and Yang R 2014 Appl. Phys. Lett. 105 131903

- [32] Cai Y, Lan J, Zhang G and Zhang Y-W 2014 Phys. Rev. B 89 35438
- [33] Yan R, Simpson J R, Bertolazzi S, Brivio J, Watson M, Wu X, Kis A, Luo T, Hight Walker A R and Xing H G 2014 ACS Nano 8 986–93
- [34] Sahoo S, Gaur A P S, Ahmadi M, Guinel M J-F and Katiyar R S 2013 J. Phys. Chem. C 117 9042–7
- [35] Liu J, Choi G-M and Cahill D G 2014 *J. Appl. Phys.* **116** 233107
- [36] Zhang X, Sun D, Li Y, Lee G-H, Cui X, Chenet D, You Y, Heinz T F and Hone J C 2015 ACS Appl. Mater. Interfaces 7 25923-9
- [37] Jiang P, Qian X, Gu X and Yang R 2017 Adv. Mater. 29 1701068
- [38] Zhang J, Hong Y, Wang X, Yue Y, Xie D, Jiang J, Xiong Y and Li P 2017 J. Phys. Chem. C 121 10336–44
- [39] Farahani H, Rajabpour A, Khanaki M and Reyhani A 2018 Comput. Mater. Sci. 142 1–6
- [40] Ong Z-Y, Cai Y and Zhang G 2016 Phys. Rev. B 94 165427
- [41] Yuan P, Li C, Xu S, Liu J and Wang X 2017 Acta Mater. 122 152–65
- [42] Taube A, Judek J, Łapińska A and Zdrojek M 2015 ACS Appl. Mater. Interfaces 7 5061–5
- [43] Hong Y, Ju M G, Zhang J and Zeng X C 2018 Phys. Chem. Chem. Phys. 20 2637–45
- [44] Venkatasubramanian R, Siivola E, Colpitts T and O'Quinn B 2001 Nature 413 597–602
- [45] Touzelbaev M N, Zhou P, Venkatasubramanian R and Goodson K E 2001 *J. Appl. Phys.* **90** 763–7
- [46] Winkler M, Liu X, König J D, Kirste L, Böttner H, Bensch W and Kienle L 2012 J. Electron. Mater. 41 1322–31
- [47] Hansen A-L, Dankwort T, Winkler M, Ditto J, Johnson D C, Koenig J D, Bartholomé K, Kienle L and Bensch W 2014 Chem. Mater. 26 6518–22
- [48] Chen P, Zhang Z, Duan X and Duan X 2018 Chem. Soc. Rev. 47 3129–51
- [49] Chiritescu C, Cahill D G, Heideman C, Lin Q, Mortensen C, Nguyen N T, Johnson D, Rostek R and Böttner H 2008 J. Appl. Phys. 104 33533
- [50] Chiritescu C, Cahill D G, Nguyen N, Johnson D, Bodapati A, Keblinski P and Zschack P 2007 Science 315 351–3
- [51] Muratore C et al 2013 Appl. Phys. Lett. 102 81604
- [52] Kim S, Zuo J M, Nguyen N T, Johnson D C and Cahill D G 2008 J. Mater. Res. 23 1064–7
- [53] Bronsema K D, De Boer J L and Jellinek F 1986 Z. Anorg. Allg. Chem. 540 15–7
- [54] Evans B L and Hazelwood R A 1971 Phys. Status Solidi 4 181–92
- [55] Kalikhman V L 1983 Inorg. Mater. 19 957-62
- [56] Brixner L H 1962 J. Inorg. Nucl. Chem. 24 257-63

- [57] Towle L C, Oberbeck V, Brown B E and Stajdohar R 1966 Science 154 895–6
- [58] Chen Z and Dames C 2015 Appl. Phys. Lett. 107 193104
- [59] Hamann D M, Bardgett D, Cordova D L M, Maynard L A, Hadland E C, Lygo A C, Wood S R, Esters M and Johnson D C 2018 Chem. Mater. 30 6209–16
- [60] Wainfan N and Parratt L G 1960 J. Appl. Phys. 31 1331-7
- [61] Fan R 2001 Chem. Mater. 13 802-5
- [62] Fan C, Yue Q, Yang J, Wei Z, Yang S and Li J 2014 Appl. Phys. Lett. 104 202105
- [63] Xenogiannopoulou E et al 2015 Nanoscale 7 7896–905
- [64] Klug H P and Alexander L E 1974 *X-Ray Diffraction Procedures* 2nd edn (New York: Wiley)
- [65] Mann J et al 2014 Adv. Mater. 26 1399-404
- [66] Kumar S and Schwingenschlögl U 2015 Chem. Mater. 27 1278–84
- [67] Cahill D G 2004 Rev. Sci. Instrum. 75 5119-22
- [68] Blinder A V, Bolgar A S and Trofimova Z A 1993 Powder Metall. Met. Ceram. 32 234–9
- [69] Bhatt R et al 2013 Appl. Phys. A 111 465-70
- [70] Pisoni A, Jacimovic J, Gaál R, Náfrádi B, Berger H, Révay Z and Forró L 2016 Scripta Materialia 114 48–50
- [71] Brixner L H and Teufer G 1963 Inorg. Chem. 2 992-6
- [72] Zhu G, Liu J, Zheng Q, Zhang R, Li D, Banerjee D and Cahill D G 2016 Nat. Commun. 7 13211
- [73] Wei X, Wang Y, Shen Y, Xie G, Xiao H, Zhong J and Zhang G 2014 Appl. Phys. Lett. 105 103902
- [74] Ding Y, Chen M and Xiao B 2016 RSC Adv. 6 7817-28
- [75] Erhart P, Hyldgaard P and Lindroth D O 2015 Chem. Mater. 27 5511–8
- [76] O'Hara K E, Hu X and Cahill D G 2001 J. Appl. Phys. 90 4852–8
- [77] Jang H, Ryder C R, Wood J D, Hersam M C and Cahill D G 2017 Adv. Mater. 29 1700650
- [78] Li D, Zhao P, Zhao J-C and Cahill D G 2013 J. Appl. Phys. 114 143102
- [79] Kuzuba T and Ishii M 1989 Phys. Status Solidi 155 K13-6
- [80] Ghosh C K, Sarkar D, Mitra M K and Chattopadhyay K K 2018 J. Phys. D: Appl. Phys. 46 395304
- [81] Gunning N S, Feser J, Beekman M, Cahill D G and Johnson D C 2015 J. Am. Chem. Soc. 137 8803–9
- [82] Gunning N S, Feser J, Falmbigl M, Beekman M, Cahill D G and Johnson D C 2014 Semicond. Sci. Technol. 29 124007
- [83] Heideman C L, Tepfer S, Lin Q, Rostek R, Zschack P, Anderson M D, Anderson I M and Johnson D C 2013 J. Am. Chem. Soc. 135 11055–62
- [84] Li Z, Bauers S R, Poudel N, Hamann D, Wang X, Choi D S, Esfarjani K, Shi L, Johnson D C and Cronin S B 2017 Nano Lett. 17 1978–86
- [85] Wu X and Luo T 2014 J. Appl. Phys. 115 14901